An orbital angular momentum-controlled hybrid nanowire circuit

Haoran Ren[1, 2, *, †], Xiaoxia Wang[3, †], Chenhao Li[1], Chenglin He[3], Yixiong Wang[3], Anlian Pan[3, *], and Stefan A. Maier[1, 4, *]

[1]Chair in Hybrid Nanosystems, Nanoinstitute Munich, Faculty of Physics, Ludwig-Maximilians-Universität München, München, 80539, Germany.

[2]MQ Photonics Research Centre, Department of Physics and Astronomy, Macquarie University, Macquarie Park NSW 2109, Australia.

[3]Key Laboratory for Micro-Nano Physics and Technology of Hunan Province, College of Materials Science and Engineering, Hunan University, Changsha 410082, People's Republic of China.

[4]Department of Physics, Imperial College London, London SW7 2AZ, United Kingdom.

*Emails: Haoran.Ren@mq.edu.au; Anlian.Pan@hnu.edu.cn;

Stefan.Maier@physik.uni-muenchen.de.

†These authors contribute equally.

ABSTRACT

Plasmonic nanostructures can enable compact multiplexing of the orbital angular momentum (OAM) of light, however, strong dissipation of the highly localized OAM-distinct plasmonic fields in the near-field region hinders on-chip OAM transmission and processing. Superior transmission efficiency is offered by semiconductor nanowires sustaining highly confined optical modes, but only the polarization degree of freedom has been utilized for their selective excitation. Here we demonstrate that incident OAM beams can selectively excite single-crystalline cadmium sulfide (CdS) nanowires, through coupling OAM-distinct plasmonic fields into nanowire waveguides for long-distance transportation. This allows us to build an OAM-controlled hybrid nanowire circuit for optical logic operations including AND and OR gates. In addition, this circuit enables on-chip photoluminescence readout of OAM-encrypted information. Our results open exciting new avenues not only for nanowire photonics to develop OAM-controlled optical switches, logic gates, and modulators, but also for OAM photonics to build ultracompact photonic circuits for information processing.

Key words: Orbital angular momentum, semiconductor nanowires, hybrid integration, photonic logic circuits, integrated photonics.

INTRODUCTION

Light may carry angular momentum induced by its polarization and spatial wavefront. The intrinsic orbital angular momentum (OAM) possessed by a helical wavefront has a theoretically unbounded set of orthogonal modes that could carry independent information channels. In addition to its fundamental role in light-matter interactions[1–6], OAM offers a promising approach to largely improving the capacity of optical devices and systems[7–15]. OAM multiplexing has thus been exploited to increase the telecommunication bandwidth for both free-space[8] and fiber-optic[9] networks, enhance security of quantum entanglement[7], and improve the capacity of holograms[12,14–17]. To realize OAM multiplexing, three schemes were developed to sort and detect OAM modes, including mode interference in real space[18], spatial filtering in momentum space[7], and log-polar[19,20] or Laguerre-Gaussian[21] mode transformation. However, these far-field approaches require a large propagation distance to produce OAM-distinct diffraction patterns, restricting the OAM detection to diffraction-limited optical systems that hinder OAM applications for integrated photonics.

Plasmonics breaks the diffraction limit by allowing subwavelength localization of light, bridging the size mismatch between high-capacity photonics and nanoscale electronics[22–24]. Nanoplasmonic detection[25–30] and demultiplexing[11,13] of OAM modes have recently been achieved through plasmonic structures designed to couple incident OAM beams into distinctive plasmonic fields. However, these OAM-distinct plasmonic fields are highly localized with strong dissipation due to metal losses[11,13,27–29], preventing them from on-chip signal transmission and processing. More critically, spatially resolving these plasmonic fields with subwavelength separation distances usually demands either a cumbersome near-field scanning optical microscope[29,31] or

a far-field high numerical aperture (NA) microscope to collect light scattering from plasmonic structures[5,11,13,25,26,28].

On the other hand, chemical synthesized free-standing nanowires, with synthesis-controlled optoelectronic properties and great flexibility for target positioning, allow highly efficient transmission of subwavelength-confined optical modes in nanowire waveguides[32–34]. As such, low-loss semiconductor nanowires, including IV (Si)[35], II-VI (CdS, ZnO)[36,37], III-V (InP, GaAs)[38,39], and newly emerged perovskite[40,41] nanowires etc., have been developed for on-chip light sources[37,42], modulators[43], and photodetectors[44], making them superior building blocks for photonic logic gates[43,45–47], integrated photonic circuits[48], and nano-processors[49,50]. To date, however, only the polarization degree of freedom of external light sources at the same frequency has been exploited to achieve selective excitation of nanowires[34,47], inevitably limiting the scope of nanowire photonics for high-capacity optical processing.

RESULTS AND DISCUSSION

Here, we demonstrate the design and construction of a new OAM-controlled hybrid nanowire circuit (OHNC) for two different photonic applications: optical logic operations and on-chip photoluminescence (PL) readout of OAM-encrypted information (Fig. 1). The OHNC device, consisted of a semi-circle-shaped plasmonic nanogroove grating and chemical synthesized CdS nanowires (Fig. 1A), allows selective excitation of nanowire waveguides through incident OAM beams with opposite topological charges (*l*). The plasmonic nanogroove grating plays two important roles: offering the mismatched linear momentum to launch surface plasmon polaritons at the metal-air interface at normal light incidence; and coupling different incident OAM beams into spatially separate and highly localized plasmonic fields.

Through precisely positioning one of end facets of nanowires to these OAM-distinct plasmonic fields, the plasmon energy of these plasmonic fields is selectively transferred to the low-loss nanowire waveguides for long-distance transportation. This strong OAM selectivity response allows us to use the OHNC device to realize AND and OR gates for optical logic operations (Fig. 1B), wherein the On and Off states of input OAM beams determine the PL output of logic gates. Furthermore, we demonstrate that the OHNC device can be used for demultiplexing OAM-encrypted images, paving the way for on-chip OAM information transmission and processing (Fig. 1C).

To achieve OAM-selective excitation of nanowire waveguides, plasmonic nanogrooves were designed to couple and sort two incident OAM beams with opposite topological charges. Without loss of generality, three types of conic sections, including the semi-circle, semi-ellipse, and semi-parabola curves, were used to formulate the design of the plasmonic nanogrooves (Fig. 2A). Mathematically, these curves are defined as: $y^2 = 2px + (e^2 - 1)x^2$, where *x* and *y* are the spatial coordinates, *p* and eccentricity *e* determine the size and shape of the curves, with *e*=0 for a circle, *e*<1 for an ellipse (*e*=0.8 in our studied case), and *e*=1 for a parabola, respectively. We numerically simulated the excitation of plasmonic fields from the three different-shaped nanogrooves engraved in a gold thin film (Fig. 2B), in which the incident light has a linear polarization along the *y* axis. Our results show that the semicircle-shaped nanogroove has advantages over the semi-ellipse- and semi-parabola-shaped ones by exhibiting stronger enhancement and tighter focusing of the OAM-distinct plasmonic fields. We selected two OAM modes of *l*=-4 and +4 in our simulation, since their produced plasmonic fields are separated by a relatively large distance (540 nm in the *x* axis), but our design can be adapted to other OAM modes through using other

mode-sorting plasmonic structures[11,13,51,52]. Previously, similar semi-circle-shaped nanogroove were successfully used to couple optical beams with different incident angles into high-loss ion-beam-milled metallic waveguides[53].

Therefore, the semi-circle-shaped nanogrooves in a grating structure were selected to investigate the coupling from OAM-distinct plasmonic fields to CdS nanowire waveguides (Figs. 2C-2D, Fig. S1). For this purpose, we used two identical CdS nanowires and positioned one of their end facets near the OAM-distinct plasmonic fields. Through adjusting the splitting angle (Θ) between the nanowires, we obtained an Θ-dependent waveguide coupling efficiency in the simulation (Fig. S2). As an example, we present simulation results of the nanowires with a splitting angle of Θ=30°, under the excitation from OAM beams of l=-4 (Fig. 2C) and +4 (Fig. 2D), respectively. Strikingly, their excited plasmonic fields are selectively coupled into the nanowire waveguides for low-loss transportation. Notably, the E_z-component of the plasmonic fields which corresponds to the transverse electric (TE) waveguide mode of the nanowires features stronger coupling strength (Figs. 2E and 2F). On the other hand, the E_x-component of plasmonic fields, dominant for the excitation of the transverse magnetic (TM) waveguide mode for nanowires with a small splitting angle (15° with respect to the y axis), shows weak coupling strength due to the y-linear polarized incident light. It should be mentioned that a similar idea of coupling of OAM-distinct surface waves into waveguide channels was recently proposed in a simulation-only paper[54].

To experimentally confirm the OAM-selective excitation of nanowires, we used the focused ion beam technique to engrave the designed semi-circle-shaped nanogroove grating in a gold thin film (see the Methods and Materials section). A gold film with a thickness of 300 nm was evaporated on an ultraflat quartz substrate using an electron-

beam evaporation process (see the Methods and Materials section). To avoid direct optical transmission and efficient conversion of the light into SPPs, the nanogrooves were optimized to have a pitch of 360 nm and a depth of 250 nm (Figs. S3 and S4, Methods). In addition, two more lines with a shallow depth of around 40 nm were further patterned to mark the nanowire positions, providing a clear guidance for our nanowire positioning in the next step (Fig. 3A). However, it should be mentioned that these engraved shallow lines might induce some plasmonic scattering loss and PL quenching in nanowires. Experimentally, CdS nanowires were synthesized by a chemical vapour deposition process (see the Methods and Materials section). Thereafter, we transferred the CdS nanowires onto the gold film and used a tapered optical fiber (Fig. 3B) to precisely position two nanowires into the marked positions. As such, we constructed an array of the designed OHNC devices, the scanning electron microscope (SEM) image of an exemplary OHNC device is given in Fig. 3C.

To experimentally characterize the OHNC devices, an optical transmission setup (Fig. S5) was built, in which a high numerical aperture (NA) lens (NA=0.8) was used to locate target devices and provide the OAM incidence. The focus of the high-NA lens was further adjusted to match the beam size with the semi-circle-shaped nanogroove grating of an OHNC device. Moreover, we placed an opaque metal plate in the back focal plane of the high-NA lens to block the direct illumination on CdS nanowires. In the transmission path, a low-NA lens (NA=0.3) was used to collect PL signals from the OHNC devices. A spatial light modulator (SLM, PLUTO-2.1, Holoeye) was used to implement compute-generated spiral phase holograms for creating different OAM modes. During the measurement, we firstly characterized the OAM-dependent spatial shifts of plasmonic fields based on nanogroove-only devices, under the illumination of different incident OAM modes ranging from -6 to +6 (Fig. S6). Not surprisingly, the

OAM-dependent plasmonic fields exhibited very small separation distances (tens of nanometers between adjacent OAM modes excitation) that are difficult to be resolved by our home-built microscope with a large magnification of 200. We then focused on the characterization of OHNC devices containing CdS nanowires, wherein strong OAM-selective excitation of nanowires was observed through the OAM-distinct PL intensity patterns (Figs. 3D-3M). In particular, the OAM incident beams of l=-4 and +4 offer a strong selective response in the excitation of nanowires on the left and right sides, respectively (Figs. 3CH-3I). Through normalizing the PL intensities for different OAM modes (from -6 to +6) with respect to the maximal OAM mode l=-4 (Fig. 3H), we found that the OAM modes l=-6, -2, -1, +1, +2, +6 create a negligible modal crosstalk (<1%), and only the adjacent OAM modes l=-+3 and -+5 have a small crosstalk of 6% and 11%, respectively. The crosstalk is defined as $I_{OAM}/I_{OAM=-4}$, where the measured PL intensities for different OAM modes (I_{OAM}) are normalized by the maximal OAM mode l=-4 ($I_{OAM=-4}$). This small OAM-multiplexing crosstalk was observed mainly because the OAM-distinct plasmonic fields are tightly focused and well separated in the near-field.

All-optical logic gates are core logic units to implement various all-optical systems for optical signal processing. Unlike conventional polarization-based logic gates in nanowire circuits[34,47], we demonstrate for the first time OAM-controlled logic gates (Fig. 4). To prove the principle, we used two OAM modes of l=-4 and +4 as the logic gate input signals, albeit our concept can be readily extended to other OAM modes. Figure 4A presents the PL spectral and microscopy images obtained from an OHNC device, under the four different combinations of OAM input signals: (1, 1), (1, 0), (0, 1), and (0, 0). Owing to the strong OAM selectivity, PL signals from the nanowires on the left and right sides can be selectively excited by these OAM modes and the associated PL

intensity can be regarded as the terminal output of our logic gates. More specifically, the PL intensity contributed from both nanowires was roughly twice as high as the case of only one of them was excited, opening the possibility to use two different intensity thresholds T_1 and T_2 (marked as dashed lines in Fig. 4A) to define AND or OR logic gates, respectively (Fig. 4B). For example, for the PL threshold T_1, the logic output becomes 1 only when both nanowires are excited (1, 1), while all other three input combinations result in an output of 0, demonstrating the behaviour of an AND gate (Fig. 4C). On the other hand, for the lower PL threshold T_2, the logic output is always 1 if at least one nanowire is excited and switched to 0 when both nanowires are dark, which behaves as an OR gate. As an example, for the intensity threshold of T_2, an OAM input (OAM_1 = 1, OAM_2 = 1) results in the PL intensity output = 1, both inputs (OAM_1 = 1, OAM_2 = 0) and (OAM_1 = 0, OAM_2 = 1) result in an output = 1, demonstrating the behaviour of an OR gate. On the other hand, if the higher intensity threshold T_1 is defined, only an input (OAM_1 = 1, OAM_2 = 1) results in an output = 1, and all the other three OAM inputs result in an output = 0, which functions as an AND gate. Notably, owing to the large amount of orthogonal OAM modes, our concept holds great promise to build more complex hybrid nanocircuit devices that feature multiple-input or multiple-output logic operators. As an example, a four-input OAM circuit can be designed based on the same semi-circle-shaped nanogroove plasmonic grating (Fig. S7).

In addition, we demonstrate that the OHNC device can be employed for on-chip readout of OAM-multiplexing-encrypted information (Fig. 5). For this purpose, we present an example in which a secret image is randomly distributed into two different shares that are encoded with distinctive OAM modes (e.g., l=-4 and +4), leading to two OAM key images (Fig. 5A). The binary information of the OAM key images was

further transferred into temporal signals of incident OAM beams, which can be experimentally implemented through a dynamic SLM with the use of a split-screen to display two spiral phase holograms. In the decryption process, the dynamically encoded OAM signal beams were superposed through a beamsplitter (Fig. S8) and incident on the OHNC device, leading to the readout of the OAM key images 1 and 2 through the nanowires on the left and right sides, respectively (Fig. 5B). Consequently, the OAM-multiplexing-encrypted secret image can be retrieved through superposing the two decoded OAM key image shares. Our approach offers a simple, powerful, and robust way for optical data protection, wherein a miniaturized OHNC device allows on-chip PL readout of OAM-multiplexing-encrypted information.

CONCLUSION

In summary, we have demonstrated the design and implementation of an OAM-controlled hybrid nanowire circuit (named here an OHNC device) through the selective coupling of OAM-distinct plasmonic fields into low-loss nanowire waveguides. To further extend the selective excitation of nanowires to other OAM modes, we envision that the principle of near-field holography[55–57] could be implemented for the design of plasmonic surface holograms, leading to a large spatial separation of OAM-distinct plasmonic fields that can further minimize the OAM-multiplexing crosstalk in the coupling to nanowires. Owing to the strong OAM-selective response, we have achieved OAM-controlled optical logic operation, which can act as AND and OR logic gates. Since the OAM degree of freedom of light has an unbounded set of orthogonal helical modes, this concept can be further extended to develop more complex hybrid nanocircuit devices harnessing multiple-input or multiple-output logic operators. Hence, we envision that incorporating the unbounded OAM modes with nanowire bandgap engineering will further expand the modulation capacity of integrated

photonic devices. Moreover, we have applied the OHNC device for on-chip PL readout of OAM-encrypted information, suggesting that the multiple use of OAM modes can significantly enhance the security of optical information. Our demonstration of an integrated OHNC device for OAM decryption could open new horizons for developing hybrid nanowire circuits for all-optical OAM information processing on-a-chip.

Comparing our work with previous OAM-based plasmonic devices[11,13], we have highlighted some key features in Table S1, including number of angular momentum modes, plasmonic incoupling and outcoupling structures (related to their coupling mechanisms), and power efficiency. Notably, previous plasmonic OAM-based devices demand either a cumbersome near-field scanning optical microscope [11,13] or a far-field high numerical aperture microscope [11,13] to distinguish highly localized OAM-coupled plasmonic fields. However, none of them allows on-chip transmission of OAM-coupled plasmonic fields, although it is crucial for integrated photonic circuits and on-chip information processing. In this paper, our designed OAM-controlled hybrid nanowire circuit allows the use of low-loss single-crystalline semiconductor nanowires to selectively transmit OAM-distinct plasmonic fields, opening the possibility of using the OAM degree of freedom for photonic logic operations and on-chip OAM information transmission and processing. In addition, unlike previous OAM-based plasmonic devices[11,13] that employed subwavelength apertures or particles for scattering OAM-coupled plasmonic fields into the far-field with a low efficiency (e.g., ~0.01%[11,13]), our hybrid nanophotonic device could offer a much higher power efficiency (~10%).

METHODS AND MATERIALS

Materials and nano-fabrication methods. A thin gold film with a thickness of 300 nm was evaporated using electron beam evaporation (Nanochrome II, Intlvac) on an ultra-

flat quartz cover slide (G380, ProSciTech) and used as our sample. The drilled semi-circle-shaped nanogroove structure with a thickness of 250 nm were fabricated in the gold film by using ion beam lithography (FEI Helios NanoLab DualBeam 650 system). To check the fabrication quality, scanning electron microscopy (SEM) imaging on the fabricated area was further carried out (FEI Helios NanoLab DualBeam 650). We numerically optimized the dimensions of nanogroove gratings to maximize the energy conversion from the incident light at normal incidence into surface plasmon polaritons (SPPs). To characterize this SPPs launching efficiency, we built a 2D numerical model in COMSOL to numerically calculate the plasmon resonance in reflection and compared the reflectance spectra with and without the nanogroove grating. Based on the refractive index data of a gold thin film[58], our numerical results suggest that the maximum value of the differential reflectance signal, which corresponds to the excitation of a plasmon resonance, can be as high as 66% at the incident wavelength of 490 nm. This allows efficient conversion of the light into SPPs and subsequent focusing into OAM-distinct plasmonic fields due to the use of semi-circle-shaped nanogrooves to focus the SPPs. The efficiency of this process strongly depends on the pitch and width of the nanogroove unit cell, with our numerically optimized values of 360 nm and 150 nm, respectively (see the inset in Fig. S4A). Based on this optimized grating structure, the SPPs field profile at the resonance frequency is presented in Fig. S4B, in which a strong field enhancement and a standing wave profile are observed.

Synthesis of CdS Nanowires. The CdS nanowires were synthesized through an Au-catalyzed chemical vapor deposition (CVD) method. An alumina boat loaded with CdS powders (Alfa Aesar, 99.999%) was put inside of centre area of a quartz tube. A 10 mm × 10 mm size silicon wafer coated with 10 nm thick Au film was mounted at the

downstream of the quartz tube in the furnace (OTF-1200X). Before heating, the quartz tube was pumped down and maintained the pressure at 300 Torr, and followed by a 50 sccm flow of high purity Ar (99.999%). Then the furnace was heated to the temperature of 760 °C within 30 min and maintained at this temperature for 120 min. After the growth, the tube was naturally cooled down to room temperature. Regarding the working efficiency of CdS nanowire waveguides, the previous work[59] reported that the working efficiency of long CdS nanoribbons are mainly determined by self-absorption loss, due to the band-tail mechanism and surface defects. For a CdS nanowire with the length less than 50 μm, the waveguiding can be very efficient and have been experimentally demonstrated with a transportation loss less than 0.02 dB/μm[48]. Therefore, the CdS nanowires (~4 μm) employed in this work should be highly efficient to transport waveguide modes with very low absorption and transmission losses.

Nanowire transfer and positioning. The optical fiber taper was drawn from a standard single mode optical fiber (SMF 28). Through using a home-built micro-operator system based on optical microscope, selected CdS nanowires with similar size were precisely transferred to the targeted positions marked during the focused ion beam milling of the OHNC devices.

ASSOCIATED CONTENT

Supporting Information

The Supporting Information is available for this paper. This Supporting Information file includes additional details about device simulation (Figs. S1, S2, S4, S7), experimental performance (Fig. S6 and Table S1), and schematics of the device (Fig. S3) and optical setups (Figs. S5 and S8).

AUTHOR INFORMATION

Author contributions: H. R., X. W., and S. A. M. proposed the idea and conceived the experiment; H. R. performed the numerical simulation; X. W., C. H., and Y. W. performed the nanofabrication and nanowire transfer; H. R. and C. L. performed the optical measurement. H. R., X. W., A. P., and S. A. M. contributed to the data analysis; H. R. wrote the manuscript with the input from all the authors.

Notes: The authors declare no competing interests.

ACKNOWLEDGEMENTS

H. R. acknowledges the funding support from the Humboldt Research Fellowship from the Alexander von Humboldt Foundation, and the Macquarie University Research Fellowship (MQRF) from Macquarie University. S. A. M. acknowledges the funding support from the Deutsche Forschungsgemeinschaft, the EPSRC (EP/M000044/1), and the Lee-Lucas Chair in Physics. C.L. acknowledges the scholarship support from the China Scholarship Council. A. P. acknowledges the funding support from the National Natural Science Foundation of China (Grant numbers: 62090035, U19A2090, and 61804052). This work was performed in part at the Melbourne Centre for Nanofabrication (MCN) in the Victorian Node of the Australian National Fabrication Facility (ANFF).

References

(1) Lavery, M. P. J.; Speirits, F. C.; Barnett, S. M.; Padgett, M. J. Detection of a Spinning Object Using Light's Orbital Angular Momentum. *Science* **2013**, *341* (6145), 537–540. https://doi.org/10.1126/science.1239936.

(2) Bliokh, K. Y.; Rodríguez-Fortuño, F. J.; Nori, F.; Zayats, A. V. Spin–Orbit Interactions of Light. *Nat Photonics* **2015**, *9* (12), 796–808. https://doi.org/10.1038/nphoton.2015.201.

(3) Forbes, K. A. Raman Optical Activity Using Twisted Photons. *Phys Rev Lett* **2019**, *122* (10), 103201. https://doi.org/10.1103/physrevlett.122.103201.

(4) Parker, J.; Peterson, C. W.; Yifat, Y.; Rice, S. A.; Yan, Z.; Gray, S. K.; Scherer, N. F. Optical Matter Machines: Angular Momentum Conversion by Collective Modes in Optically Bound Nanoparticle Arrays. *Optica* **2020**, *7* (10), 1341. https://doi.org/10.1364/optica.396147.

(5) Ren, H.; Gu, M. Angular Momentum-Reversible Near-Unity Bisignate Circular Dichroism. *Laser Photonics Rev* **2018**, *12* (5), 1700255. https://doi.org/10.1002/lpor.201700255.

(6) Zhang, M.; Ren, H.; Ouyang, X.; Jiang, M.; Lu, Y.; Hu, Y.; Fu, S.; Li, Z.; Chen, Z.; Guan, B.-O.; Cao, Y.; Li, X. Nanointerferometric Discrimination of the Spin–Orbit Hall Effect. *Acs Photonics* **2021**, *8* (4), 1169–1174. https://doi.org/10.1021/acsphotonics.1c00087.

(7) Mair, A.; Vaziri, A.; Weihs, G.; Zeilinger, A. Entanglement of the Orbital Angular Momentum States of Photons. *Nature* **2001**, *412* (6844), 313–316. https://doi.org/10.1038/35085529.

(8) Wang, J.; Yang, J.-Y.; Fazal, I. M.; Ahmed, N.; Yan, Y.; Huang, H.; Ren, Y.; Yue, Y.; Dolinar, S.; Tur, M.; Willner, A. E. Terabit Free-Space Data Transmission Employing Orbital Angular Momentum Multiplexing. *Nat Photonics* **2012**, *6* (7), 488–496. https://doi.org/10.1038/nphoton.2012.138.

(9) Bozinovic, N.; Yue, Y.; Ren, Y.; Tur, M.; Kristensen, P.; Huang, H.; Willner, A. E.; Ramachandran, S. Terabit-Scale Orbital Angular Momentum Mode Division Multiplexing in Fibers. *Science* **2013**, *340* (6140), 1545–1548. https://doi.org/10.1126/science.1237861.

(10) Willner, A. E.; Zhao, Z.; Liu, C.; Zhang, R.; Song, H.; Pang, K.; Manukyan, K.; Song, H.; Su, X.; Xie, G.; Ren, Y.; Yan, Y.; Tur, M.; Molisch, A. F.; Boyd, R. W.; Zhou, H.; Hu, N.; Minoofar, A.; Huang, H. Perspectives on Advances in High-Capacity, Free-Space Communications Using Multiplexing of Orbital-Angular-Momentum Beams. *Apl Photonics* **2021**, *6* (3), 030901. https://doi.org/10.1063/5.0031230.

(11) Yue, Z.; Ren, H.; Wei, S.; Lin, J.; Gu, M. Angular-Momentum Nanometrology in an Ultrathin Plasmonic Topological Insulator Film. *Nat Commun* **2018**, *9* (1), 4413. https://doi.org/10.1038/s41467-018-06952-1.

(12) Ren, H.; Briere, G.; Fang, X.; Ni, P.; Sawant, R.; Héron, S.; Chenot, S.; Vézian, S.; Damilano, B.; Brändli, V.; Maier, S. A.; Genevet, P. Metasurface Orbital Angular Momentum Holography. *Nat Commun* **2019**, *10* (1), 2986. https://doi.org/10.1038/s41467-019-11030-1.

(13) Ren, H.; Li, X.; Zhang, Q.; Gu, M. On-Chip Noninterference Angular Momentum Multiplexing of Broadband Light. *Science* **2016**, *352* (6287), 805–809. https://doi.org/10.1126/science.aaf1112.

(14) Fang, X.; Ren, H.; Gu, M. Orbital Angular Momentum Holography for High-Security Encryption. *Nat Photonics* **2020**, *14* (2), 102–108. https://doi.org/10.1038/s41566-019-0560-x.

(15) Ren, H.; Fang, X.; Jang, J.; Bürger, J.; Rho, J.; Maier, S. A. Complex-Amplitude Metasurface-Based Orbital Angular Momentum Holography in Momentum Space. *Nat Nanotechnol* **2020**, *15* (11), 948–955. https://doi.org/10.1038/s41565-020-0768-4.

(16) Li, C.; Maier, S. A., Ren, H. Optical Vortices in Nanophotonics. *Chin. Opt.* **2021**, *14* (4), 1–20. https://doi.org/10.37188/co.2021-0066.

(17) Piccardo, M.; Ginis, V.; Forbes, A.; Mahler, S.; Friesem, A. A.; Davidson, N.; Ren, H.; Dorrah, A. H.; Capasso, F.; Dullo, F. T.; Ahluwalia, B. S.; Ambrosio, A.; Gigan, S.; Treps, N.; Hiekkamäki, M.; Fickler, R.; Kues, M.; Moss, D.; Morandotti, R.; Riemensberger, J.; Kippenberg, T. J.; Faist, J.; Scalari, G.; Picqué, N.; Hänsch, T. W.; Cerullo, G.; Manzoni, C.; Lugiato, L. A.; Brambilla, M.; Columbo, L.; Gatti, A.; Prati, F.; Shiri, A.; Abouraddy, A. F.; Alù, A.; Galiffi, E.; Pendry, J. B.; Huidobro, P. A. Roadmap on Multimode Light Shaping. *Arxiv* **2021**. URL: arXiv:2104.03550 (Accessed 2021-04-08).

(18) Allen, L.; Beijersbergen, M. W.; Spreeuw, R. J. C.; Woerdman, J. P. Orbital Angular Momentum of Light and the Transformation of Laguerre-Gaussian Laser Modes. *Phys Rev A* **1992**, *45* (11), 8185–8189. https://doi.org/10.1103/physreva.45.8185.

(19) Berkhout, G. C. G.; Lavery, M. P. J.; Courtial, J.; Beijersbergen, M. W.; Padgett, M. J. Efficient Sorting of Orbital Angular Momentum States of Light. *Phys Rev Lett* **2010**, *105* (15), 153601. https://doi.org/10.1103/physrevlett.105.153601.

(20) Mirhosseini, M.; Malik, M.; Shi, Z.; Boyd, R. W. Efficient Separation of the Orbital Angular Momentum Eigenstates of Light. *Nat Commun* **2013**, *4* (1), 2781. https://doi.org/10.1038/ncomms3781.

(21) Fontaine, N. K.; Ryf, R.; Chen, H.; Neilson, D. T.; Kim, K.; Carpenter, J. Laguerre-Gaussian Mode Sorter. *Nat Commun* **2019**, *10* (1), 1865. https://doi.org/10.1038/s41467-019-09840-4.

(22) Maier, S. A. *Plasmonics: Fundamentals and Applications*; Springer Science & Business Media: New York, **2007**.

(23) Gramotnev, D. K.; Bozhevolnyi, S. I. Plasmonics beyond the Diffraction Limit. *Nat Photonics* **2010**, *4* (2), 83–91. https://doi.org/10.1038/nphoton.2009.282.

(24) Ozbay, E. Plasmonics: Merging Photonics and Electronics at Nanoscale Dimensions. *Science* **2006**, *311* (5758), 189–193. https://doi.org/10.1126/science.1114849.

(25) Garoli, D.; Zilio, P.; Gorodetski, Y.; Tantussi, F.; Angelis, F. D. Beaming of Helical Light from Plasmonic Vortices via Adiabatically Tapered Nanotip. *Nano Lett* **2016**, *16* (10), 6636–6643. https://doi.org/10.1021/acs.nanolett.6b03359.

(26) Gorodetski, Y.; Drezet, A.; Genet, C.; Ebbesen, T. W. Generating Far-Field Orbital Angular Momenta from Near-Field Optical Chirality. *Phys Rev Lett* **2012**, *110* (20), 203906. https://doi.org/10.1103/physrevlett.110.203906.

(27) Genevet, P.; Lin, J.; Kats, M. A.; Capasso, F. Holographic Detection of the Orbital Angular Momentum of Light with Plasmonic Photodiodes. *Nat Commun* **2012**, *3* (1), 1278. https://doi.org/10.1038/ncomms2293.

(28) Gorodetski, Y.; Shitrit, N.; Bretner, I.; Kleiner, V.; Hasman, E. Observation of Optical Spin Symmetry Breaking in Nanoapertures. *Nano Lett* **2009**, *9* (8), 3016–3019. https://doi.org/10.1021/nl901437d.

(29) Mei, S.; Huang, K.; Liu, H.; Qin, F.; Mehmood, M. Q.; Xu, Z.; Hong, M.; Zhang, D.; Teng, J.; Danner, A.; Qiu, C.-W. On-Chip Discrimination of Orbital Angular Momentum of Light with Plasmonic Nanoslits. *Nanoscale* **2015**, *8* (4), 2227–2233. https://doi.org/10.1039/c5nr07374j.

(30) Tsai, W.-Y.; Huang, J.-S.; Huang, C.-B. Selective Trapping or Rotation of Isotropic Dielectric Microparticles by Optical Near Field in a Plasmonic Archimedes Spiral. *Nano Lett* **2014**, *14* (2), 547–552. https://doi.org/10.1021/nl403608a.

(31) Liu, A.-P.; Xiong, X.; Ren, X.-F.; Cai, Y.-J.; Rui, G.-H.; Zhan, Q.-W.; Guo, G.-C.; Guo, G.-P. Detecting Orbital Angular Momentum through Division-of-Amplitude Interference with a Circular Plasmonic Lens. *Sci Rep-uk* **2013**, *3* (1), 2402. https://doi.org/10.1038/srep02402.

(32) Oulton, R. F.; Sorger, V. J.; Genov, D. A.; Pile, D. F. P.; Zhang, X. A Hybrid Plasmonic Waveguide for Subwavelength Confinement and Long-Range Propagation. *Nat Photonics* **2008**, *2* (8), 496–500. https://doi.org/10.1038/nphoton.2008.131.

(33) Fang, Y.; Sun, M. Nanoplasmonic Waveguides: Towards Applications in Integrated Nanophotonic Circuits. *Light Sci Appl* **2015**, *4* (6), e294–e294. https://doi.org/10.1038/lsa.2015.67.

(34) Yan, Y.; Zhang, C.; Zheng, J. Y.; Yao, J.; Zhao, Y. S. Optical Modulation Based on Direct Photon-Plasmon Coupling in Organic/Metal Nanowire Heterojunctions. *Adv Mater* **2012**, *24* (42), 5681–5686. https://doi.org/10.1002/adma.201202698.

(35) Mølhave, K.; Wacaser, B. A.; Petersen, D. H.; Wagner, J. B.; Samuelson, L.; Bøggild, P. Epitaxial Integration of Nanowires in Microsystems by Local Micrometer-Scale Vapor-Phase Epitaxy. *Small* **2008**, *4* (10), 1741–1746. https://doi.org/10.1002/smll.200800366.

(36) Barrelet, C. J.; Wu, Y.; Bell, D. C.; Lieber, C. M. Synthesis of CdS and ZnS Nanowires Using Single-Source Molecular Precursors. *J Am Chem Soc* **2003**, *125* (38), 11498–11499. https://doi.org/10.1021/ja036990g.

(37) Huang, M. H.; Mao, S.; Feick, H.; Yan, H.; Wu, Y.; Kind, H.; Weber, E.; Russo, R.; Yang, P. Room-Temperature Ultraviolet Nanowire Nanolasers. *Science* **2001**, *292* (5523), 1897–1899. https://doi.org/10.1126/science.1060367.

(38) Johansson, J.; Karlsson, L. S.; Svensson, C. P. T.; Mårtensson, T.; Wacaser, B. A.; Deppert, K.; Samuelson, L.; Seifert, W. Structural Properties of 〈111〉B - Oriented III–V Nanowires. *Nat Mater* **2006**, *5* (7), 574–580. https://doi.org/10.1038/nmat1677.

(39) Mårtensson, T.; Wagner, J. B.; Hilner, E.; Mikkelsen, A.; Thelander, C.; Stangl, J.; Ohlsson, B. J.; Gustafsson, A.; Lundgren, E.; Samuelson, L.; Seifert, W. Epitaxial Growth of Indium Arsenide Nanowires on Silicon Using Nucleation Templates Formed by Self-Assembled Organic Coatings. *Adv Mater* **2007**, *19* (14), 1801–1806. https://doi.org/10.1002/adma.200700285.

(40) Zhu, H.; Fu, Y.; Meng, F.; Wu, X.; Gong, Z.; Ding, Q.; Gustafsson, M. V.; Trinh, M. T.; Jin, S.; Zhu, X.-Y. Lead Halide Perovskite Nanowire Lasers with Low Lasing Thresholds and High Quality Factors. *Nat Mater* **2015**, *14* (6), 636–642. https://doi.org/10.1038/nmat4271.

(41) Wang, X.; Shoaib, M.; Wang, X.; Zhang, X.; He, M.; Luo, Z.; Zheng, W.; Li, H.; Yang, T.; Zhu, X.; Ma, L.; Pan, A. High-Quality In-Plane Aligned CsPbX 3 Perovskite Nanowire Lasers with Composition-Dependent Strong Exciton–Photon Coupling. *Acs Nano* **2018**, *12* (6), 6170–6178. https://doi.org/10.1021/acsnano.8b02793.

(42) Saxena, D.; Mokkapati, S.; Parkinson, P.; Jiang, N.; Gao, Q.; Tan, H. H.; Jagadish, C. Optically Pumped Room-Temperature GaAs Nanowire Lasers. *Nat Photonics* **2013**, *7* (12), 963–968. https://doi.org/10.1038/nphoton.2013.303.

(43) Piccione, B.; Cho, C.-H.; Vugt, L. K. van; Agarwal, R. All-Optical Active Switching in Individual Semiconductor Nanowires. *Nat Nanotechnol* **2012**, *7* (10), 640–645. https://doi.org/10.1038/nnano.2012.144.

(44) Gibson, S. J.; Kasteren, B. van; Tekcan, B.; Cui, Y.; Dam, D. van; Haverkort, J. E. M.; Bakkers, E. P. A. M.; Reimer, M. E. Tapered InP Nanowire Arrays for Efficient Broadband High-Speed Single-Photon Detection. *Nat Nanotechnol* **2019**, *14* (5), 473–479. https://doi.org/10.1038/s41565-019-0393-2.

(45) Wei, H.; Wang, Z.; Tian, X.; Käll, M.; Xu, H. Cascaded Logic Gates in Nanophotonic Plasmon Networks. *Nat Commun* **2011**, *2* (1), 387. https://doi.org/10.1038/ncomms1388.

(46) Huang, Y.; Duan, X.; Cui, Y.; Lauhon, L. J.; Kim, K.-H.; Lieber, C. M. Logic Gates and Computation from Assembled Nanowire Building Blocks. *Science* **2001**, *294* (5545), 1313–1317. https://doi.org/10.1126/science.1066192.

(47) Yang, H.; Khayrudinov, V.; Dhaka, V.; Jiang, H.; Autere, A.; Lipsanen, H.; Sun, Z.; Jussila, H. Nanowire Network–Based Multifunctional All-Optical Logic Gates. *Sci Adv* **2018**, *4* (7), eaar7954. https://doi.org/10.1126/sciadv.aar7954.

(48) Barrelet, C. J.; Greytak, A. B.; Lieber, C. M. Nanowire Photonic Circuit Elements. *Nano Lett* **2004**, *4* (10), 1981–1985. https://doi.org/10.1021/nl048739k.

(49) Park, H.-G.; Barrelet, C. J.; Wu, Y.; Tian, B.; Qian, F.; Lieber, C. M. A Wavelength-Selective Photonic-Crystal Waveguide Coupled to a Nanowire Light Source. *Nat Photonics* **2008**, *2* (10), 622–626. https://doi.org/10.1038/nphoton.2008.180.

(50) Yan, H.; Choe, H. S.; Nam, S.; Hu, Y.; Das, S.; Klemic, J. F.; Ellenbogen, J. C.; Lieber, C. M. Programmable Nanowire Circuits for Nanoprocessors. *Nature* **2011**, *470* (7333), 240–244. https://doi.org/10.1038/nature09749.

(51) Feng, F.; Si, G.; Min, C.; Yuan, X.; Somekh, M. On-Chip Plasmonic Spin-Hall Nanograting for Simultaneously Detecting Phase and Polarization Singularities. *Light Sci Appl* **2020**, *9* (1), 95. https://doi.org/10.1038/s41377-020-0330-z.

(52) Chen, J.; Chen, X.; Li, T.; Zhu, S. On-Chip Detection of Orbital Angular Momentum Beam by Plasmonic Nanogratings. *Laser Photonics Rev* **2018**, *12* (8), 1700331. https://doi.org/10.1002/lpor.201700331.

(53) Imre, A.; Vlasko-Vlasov, V. K.; Pearson, J.; Hiller, J. M.; Welp, U. Multiplexing Surface Plasmon Polaritons on Nanowires. *Appl Phys Lett* **2007**, *91* (8), 083115. https://doi.org/10.1063/1.2773992.

(54) Ye, J.; Li, Y.; Qu, S. On-Chip Orbital Angular Momentum Sorting With a Surface Plasmon Polariton Lens. *J Lightwave Technol* **2020**, *39* (5), 1423–1428. https://doi.org/10.1109/jlt.2020.3039270.

(55) Genevet, P.; Capasso, F. Holographic Optical Metasurfaces: A Review of Current Progress. *Rep Prog Phys* **2015**, *78* (2), 024401. https://doi.org/10.1088/0034-4885/78/2/024401.

(56) Ginis, V.; Piccardo, M.; Tamagnone, M.; Lu, J.; Qiu, M.; Kheifets, S.; Capasso, F. Remote Structuring of Near-Field Landscapes. *Science* **2020**, *369* (6502), 436–440. https://doi.org/10.1126/science.abb6406.

(57) Epstein, I.; Lilach, Y.; Arie, A. Shaping Plasmonic Light Beams with Near-Field Plasmonic Holograms. *J Opt Soc Am B* **2014**, *31* (7), 1642. https://doi.org/10.1364/josab.31.001642.

(58) Rosenblatt, G.; Simkhovich, B.; Bartal, G.; Orenstein, M. Nonmodal Plasmonics: Controlling the Forced Optical Response of Nanostructures. *Phys Rev X* **2020**, *10* (1), 011071. https://doi.org/10.1103/physrevx.10.011071.

(59) Pan, A.; Liu, D.; Liu, R.; Wang, F.; Zhu, X.; Zou, B. Optical Waveguide through CdS Nanoribbons. *Small* **2005**, *1* (10), 980–983. https://doi.org/10.1002/smll.200500112.

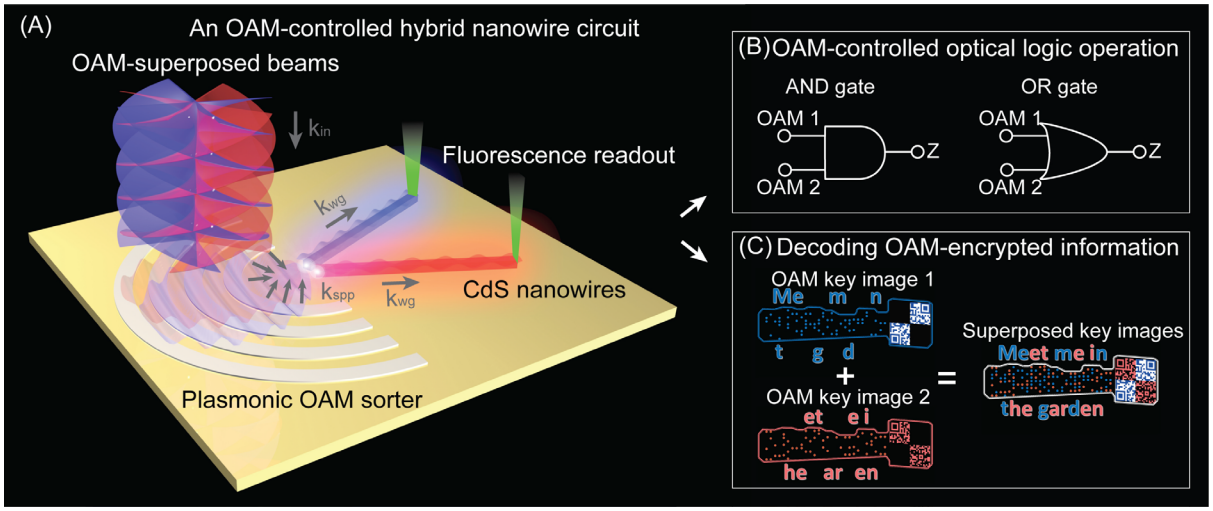


Figure 1. Schematic illustration of an OAM-controlled hybrid nanowire circuit (OHNC). (**A**) Schematic of an OHNC device, consisting of a semi-circle-shaped plasmonic nanogroove grating and chemical synthesized CdS nanowires. The OHNC selectively couples two OAM-superposed beams with opposite topological charges into two different nanowire waveguides. (**B** and **C**) Photonic applications of the OHNC for OAM-controlled optical logic operation (B) and on-chip demultiplexing OAM-encrypted information (C). In (A), we marked the propagation directions of incident OAM beams (k_{in}), excited surface plasmon polaritons (k_{spp}), and coupled waveguide modes (k_{wg}), respectively.

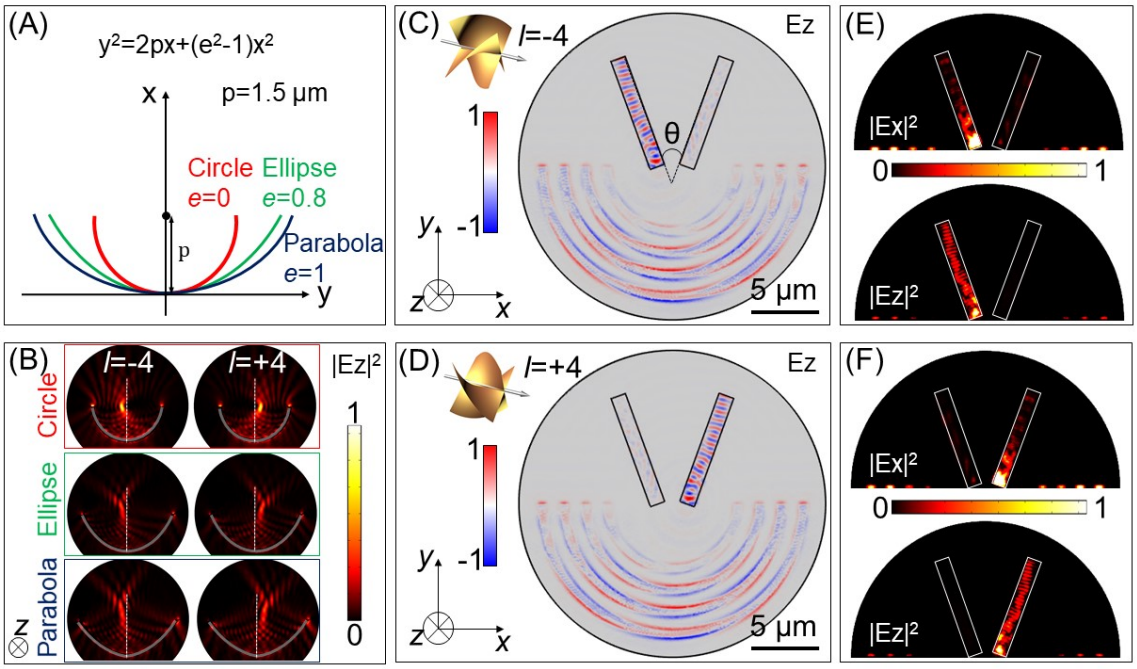


Figure 2. Design principle of an OHNC device. (**A**) Geometric comparison of three different types of conic sections, including the semi-circle, semi-ellipse, and semi-parabola curves, which can be used to formulate the design of plasmonic nanogrooves. (**B**) Numerical simulation of the excitation of plasmonic fields based on the above different-shaped nanogrooves engraved in a gold thin film. (**C** and **D**) Theoretical demonstration of OAM-selective excitation of CdS nanowires, under the illumination of OAM modes of l=-4 (C) and l=+4 (D), respectively. (**E** and **F**) Numerical study of the coupling of the E_x- and E_z-components of plasmonic fields into the nanowire waveguides, under the illumination of OAM modes of *l*=-4 (E) and l=+4 (F), respectively.

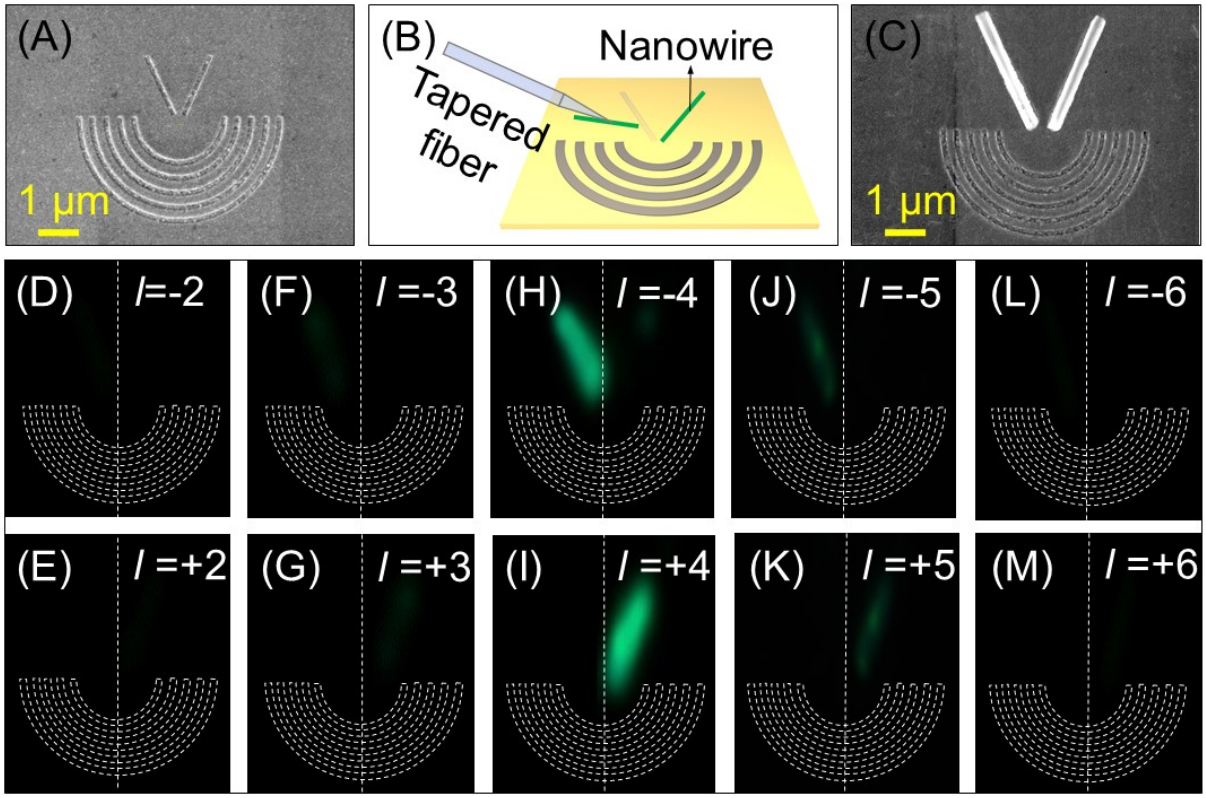
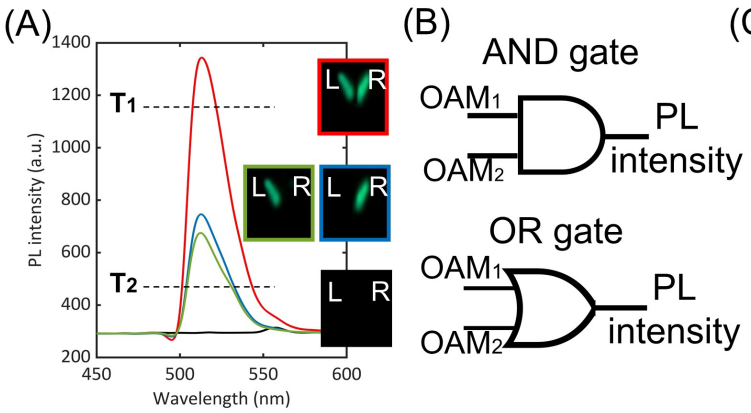


Figure 3. Experimental characterization of the OAM-selective excitation of nanowires. (**A**) SEM image of a fabricated plasmonic structure before the nanowire transfer. (**B**) Schematic illustration of spatial positioning of chemical synthesized nanowires using a tapered optical fiber. (**C**) SEM image of the OHNC device, with transferred nanowires. (**D-M**) Experimental characterization of the OHNC device through collecting the PL microscope images from the nanowires, exhibiting strong OAM-selective excitation of nanowires based on the OAM modes of *l*=-4 (H) and +4 (I).



(C)

OAM_1 (l=-4)	OAM_2 (l=+4)	AND (T_1)	OR(T_2)
1	1	1	1
1	0	0	1
0	1	0	1
0	0	0	0

Figure 4. Demonstration of OAM-controlled logic gates. (**A**) PL spectral and microscopy images obtained from an OHNC device, under four different combinations of OAM input signals (l=-4 and +4): (1, 1), (1, 0), (0, 1), and (0, 0). T_1 and T_2 are marked PL intensity thresholds to define AND and OR logic gates, respectively. (**B**) Schematic of AND and OR gates based on OAM inputs and PL intensity output. (**C**) Summary of optical logic operations for AND and OR gates based on the PL intensity thresholds T_1 and T_2, respectively.

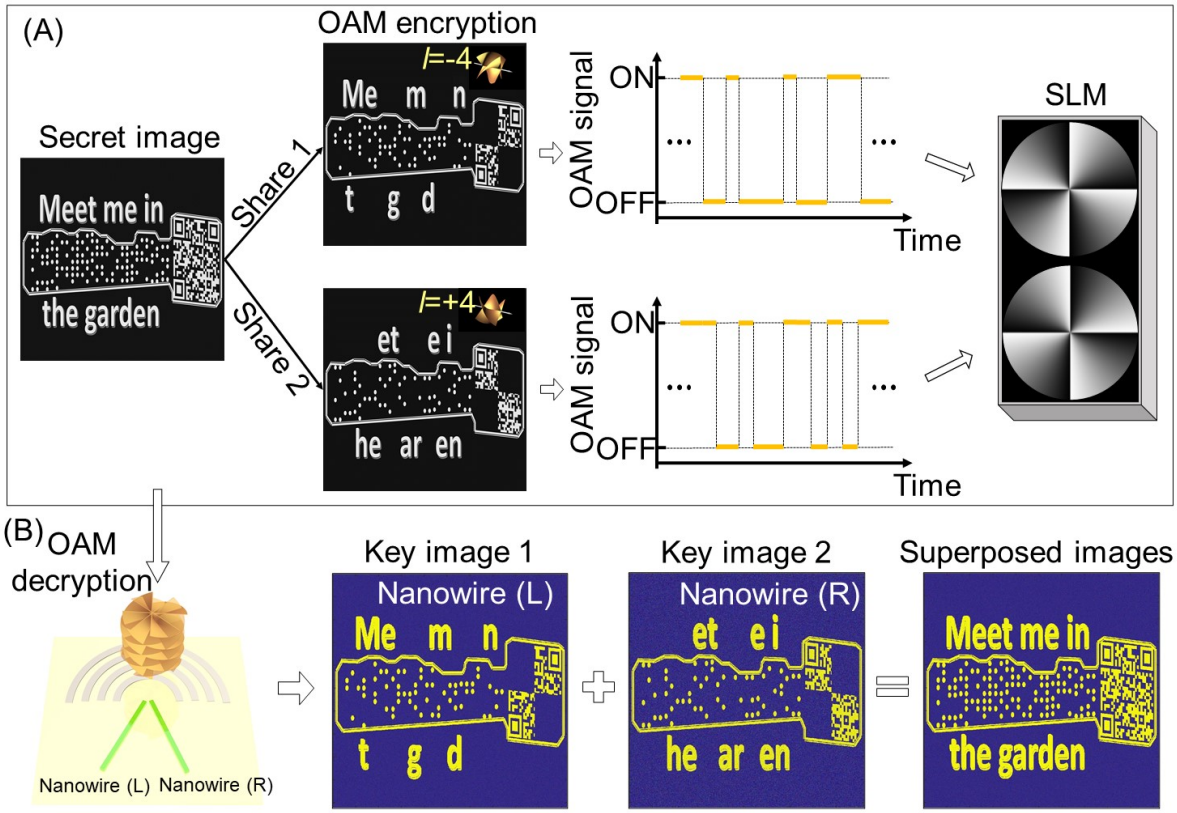
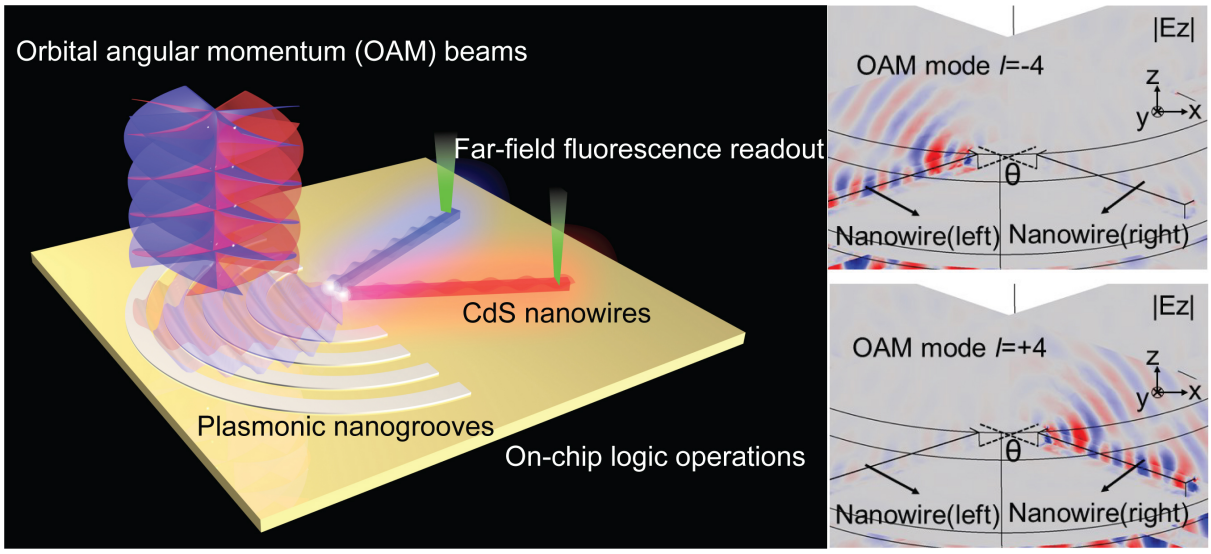


Figure 5. Experimental demonstration of using the OHNC device for on-chip decryption of OAM-multiplexing-encrypted information. (**A**) Schematic illustration of the process of OAM encryption, through randomly distributing a secret image into two different shares that are encoded with distinctive OAM modes. Generation of the two OAM key images were experimentally realized through a split-screen SLM with two spiral phase holograms to produce the OAM modes of *l*=-4 and +4. (**B**) Experimentally retrieved OAM key images 1 and 2 through the left- and right-side nanowires in an OHNC device, respectively, superposed of which leads to the original OAM-multiplexing-encrypted secret image.

TOC Graphic.


Orbital angular momentum (OAM) beams
Far-field fluorescence readout
CdS nanowires
Plasmonic nanogrooves
On-chip logic operations
|Ez|
OAM mode l=-4
z
y
x
θ
Nanowire(left)
Nanowire(right)
|Ez|
OAM mode l=+4
z
y
x
θ
Nanowire(left)
Nanowire(right)